

# Proceedings of the Institution of Mechanical Engineers, Part C: Journal of Mechanical Engineering Science

<http://pic.sagepub.com/>

---

## **Contact and elasto-hydrodynamic analysis of worm gears Part 1: Theoretical formulation**

K. J. Sharif, S Kong, H. P. Evans and R. W. Snidle

*Proceedings of the Institution of Mechanical Engineers, Part C: Journal of Mechanical Engineering Science* 2001  
215: 817

DOI: 10.1243/0954406011524171

The online version of this article can be found at:

<http://pic.sagepub.com/content/215/7/817>

---

Published by:



<http://www.sagepublications.com>

On behalf of:



[Institution of Mechanical Engineers](http://www.institutionofmechanicalengineers.org)

**Additional services and information for *Proceedings of the Institution of Mechanical Engineers, Part C: Journal of Mechanical Engineering Science* can be found at:**

**Email Alerts:** <http://pic.sagepub.com/cgi/alerts>

**Subscriptions:** <http://pic.sagepub.com/subscriptions>

**Reprints:** <http://www.sagepub.com/journalsReprints.nav>

**Permissions:** <http://www.sagepub.com/journalsPermissions.nav>

**Citations:** <http://pic.sagepub.com/content/215/7/817.refs.html>

>> [Version of Record](#) - Jul 1, 2001

[What is This?](#)

# Contact and elastohydrodynamic analysis of worm gears

## Part 1: theoretical formulation

K J Sharif, S Kong, H P Evans and R W Snidle\*

Cardiff School of Engineering, Cardiff University, Wales, UK

**Abstract:** The paper presents the theoretical basis for modelling the contact conditions and elastohydrodynamic lubrication (EHL) of worm gears, the results of which are presented in Part 2. The asymmetric elongated contact that typifies worm gears is non-Hertzian and is treated using a novel three-dimensional elastic contact simulation technique. The kinematic conditions at the EHL contact are such that the surfaces have a slide–roll ratio equal to almost 2, and the sliding direction varies over the contact area. These considerations require a non-Newtonian, thermal analysis, and the appropriate form of a novel Reynolds equation is developed that can incorporate any form of the non-Newtonian relationship between shear stress and strain rate. A form that incorporates both limiting shear stress and Eyring shear thinning is utilized in which the two effects can be included both singly or together.

**Keywords:** worm gears, elastohydrodynamic, thermal, non-Newtonian

### NOTATION

$a$	contact semi-dimension (m)	$U$	fluid velocity in the $x$ direction (m/s)
$A$	area subject to lubricant pressure (m <sup>2</sup> )	$\bar{U}$	mean surface velocity in the $x$ direction (m/s)
$c$	specific heat (J/kg K)	$v$	fluid velocity in the $r$ direction (m/s)
$C, D$	flow factors in the non-Newtonian Reynolds equation (ms)	$\bar{v}$	mean surface velocity in the $r$ direction (m/s)
$E'$	reduced elastic modulus (Pa)	$V$	fluid velocity in the $y$ direction (m/s)
$h$	film thickness (m)	$\bar{V}$	mean surface velocity in the $y$ direction (m/s)
$h_u$	undeformed film shape (m)	$W$	load (N)
$h_0$	load-determining constant in the film thickness equation(m)	$x$	Cartesian coordinate in the contact plane (m)
$k$	thermal conductivity (W/m K)	$x', y'$	dummy variables in the deflection integral (m)
$p$	pressure (Pa)	$y$	Cartesian coordinate in the contact plane (m)
$p_r$	$\partial p / \partial r$	$\dot{\gamma}$	shear strain rate (s <sup>-1</sup> )
$p_s$	$\partial p / \partial s$	$\varepsilon$	oil thermal expansivity (K <sup>-1</sup> )
$q$	heat flux at the solid boundary (W/m <sup>2</sup> )	$\eta$	absolute viscosity (Pa s)
$r$	coordinate in the local non-sliding direction (m)	$\theta$	temperature (K)
$s$	coordinate in the local sliding direction (m)	$\theta_{\text{ref}}$	bulk temperature of the component (K)
$t$	time of heating (s)	$\theta_0$	reference temperature for the viscosity relationship (K)
$u$	fluid velocity in the $s$ direction (m/s)	$\lambda$	dummy variable in the surface temperature integral (s)
$\bar{u}$	mean surface velocity in the $s$ direction (m/s)	$\rho$	density (kg/m <sup>3</sup> )
		$\tau$	shear stress (Pa)
		$\tau_L$	limiting shear stress (Pa)
		$\tau_0$	Eyring shear stress (limit of Newtonian behaviour) (Pa)
		$\phi$	angle between the $x$ and $s$ directions

The MS was received on 16 November 2000 and was accepted after revision for publication on 17 April 2001.

\*Corresponding author: Cardiff School of Engineering, Mechanical Engineering and Energy Studies Division, Cardiff University, Queen's Buildings, The Parade, PO Box 925, Cardiff CF24 0YF, Wales, UK.

## 1 INTRODUCTION

Worm gears, as shown in Fig. 1, provide a simple and cost effective solution in power transmission applications where a high reduction ratio is required in relatively slow-speed drives. Comparable parallel axis gearing would normally require two or three stages to achieve the same reductions with a consequent increase in complexity and number of parts. Worm drives are widely used in industry for process machinery, conveyors, elevators, etc. The main disadvantages of worm gearing are lubrication and wear problems due to the relatively high degree of sliding at the tooth contacts. In order to avoid scuffing (welding and tearing of the tooth surfaces caused by lubrication breakdown) it has so far been necessary to use metallurgically dissimilar materials for the worm and wheel. Traditionally, a steel worm and phosphor bronze wheel are used. Cast iron has also been tried as a wheel material but is generally less resistant to scuffing than bronze. However, the use of a relatively soft material for one of the surfaces limits allowable contact stresses and hence load capacity. Existing worm drives therefore tend to have a low power-weight ratio compared with conventional gearing where hardened steel can be used for both contacting surfaces.

The high degree of sliding coupled with unfavourable hydrodynamic conditions leads to relatively low efficiency and a poor thermal rating compared with conventional gearing. The mechanical efficiency of typical high-ratio designs can be as low as 70–80 per cent compared with figures of 95 per cent or better for parallel axis units [1]. These well-known drawbacks of worm drives have been tolerated in the past because of their simplicity and low initial cost. In a more compe-

titive gearing world, however, the power-weight ratio and thermal rating are becoming more important as selling points, and there is a need to upgrade traditional worm gearing technology with the aim of improving load capacity and efficiency.

Part of the required improvement in worm gearing technology can be made on the basis of a better understanding of the contact geometry and contact stresses and the way in which these are influenced by design, manufacturing accuracy, elastic distortion and the wear that occurs during operation. This is the subject of tooth contact analysis (TCA), and advances in the understanding of this aspect of worm design have been made recently by Litvin and Kin [2], Seol and Litvin [3], Fang and Tsay [4], Hu [5] and Su *et al.* [6]. The second important aspect of worm gearing is the known, poor elastohydrodynamic lubrication (EHL) performance of the contacts between worm and wheel teeth. Bathgate and Yates [7] applied elementary line contact EHL theory to a worm gear together with calculations of flash and total contact temperature. Discharge voltage measurements of film thickness gave values in the range 0.03–0.3  $\mu\text{m}$  with the particular oil used. Fuan *et al.* [8] also applied line contact EHL theory to a worm gear and predicted film thickness values of 0–2.5  $\mu\text{m}$ , and concluded that lubrication in the middle part of the contact area is weak because of poor entrainment conditions in this region. Detailed results for EHL modelling of worm contacts have not appeared in the literature, although Simon [9, 10] has presented performance curves in terms of non-dimensional flash temperature, EHL load-carrying capacity and friction factor ratios derived from such analyses. The high ratio of sliding to rolling velocity at the contacts, combined with what appears to be a relatively unfavourable entraining geometry of typical designs, gives poor film-forming characteristics and leads to the main limitations of low load capacity and low efficiency. Of particular interest is the hard steel worm/hard steel wheel combination that is now being considered as a serious alternative to the traditional steel/bronze design as a means of dramatically improving load capacity provided that the lubrication conditions at the tooth contacts can be improved.

One of the aims of the project, of which the present study forms a part, is to investigate the geometrical and kinematic design factors that influence hydrodynamic film forming in worms, and to optimize, if possible, these factors in combination with contact stressing and ease of manufacture. Such an integrated approach to improvement of worm gearing technology depends upon a thorough understanding of contact mechanics and hydrodynamic lubrication of the concentrated contacts. The present paper reports on the study of a particular worm gear design and the aim is to show the general features of the tooth contact in terms of elastostatic and elastohydrodynamic behaviour.

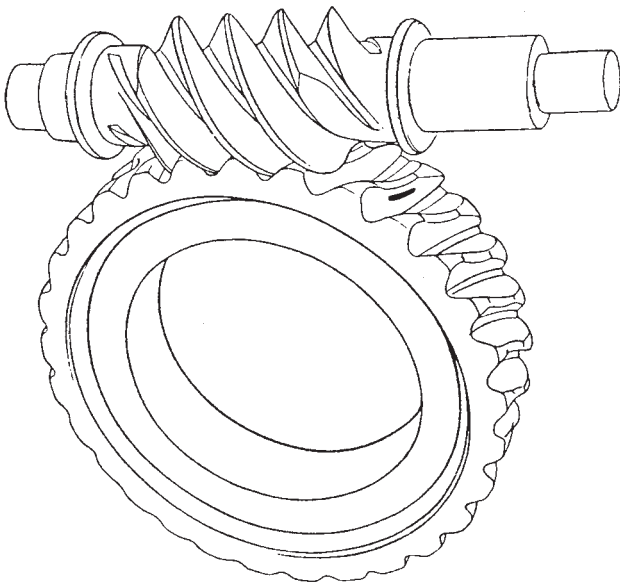


Fig. 1 Worm and wheel pair

The worm gears examined in this study are of the standard 'ZI' type. In this system the worm is an involute helicoid. The geometry of the mating wheel is generated from a cutting hob of nominally the same geometry as the worm. In the case where worm and hob are exactly the same, the meshing action is conjugate with contact occurring at a line. However, in order to provide an inlet clearance at the contact to facilitate the generation of an oil film and prevent damaging edge contacts, the hob is usually chosen to be 'oversize' which means that under unloaded conditions the contact occurs at a point rather than at a line. The process of generation of this non-conjugate geometry of the wheel surface is accomplished by a numerical simulation. A technique for this purpose is described by Hu [5] and is adopted in the present work.

## 2 CONTACT ANALYSIS

An elastic contact analysis based on semi-infinite body deflections was developed to determine the shape and extent of the dry contact area between the wheel and worm under load [11]. The shape of the gap between the two components when touching under zero load is taken as  $h_u(x, y)$ , where the  $x$  and  $y$  axes lie in the contact tangent plane. The shape of the gap between the bodies under the action of pressure  $p(x, y)$  is then

$$h(x, y) = h_u(x, y) + \frac{2}{\pi E'} \iint_A \frac{p(x', y')}{\sqrt{(x' - x)^2 + (y' - y)^2}} dx' dy' \quad (1)$$

The contact analysis method is an extension of the simple line contact method presented by Snidle and Evans [12]. In essence, a target deflection  $h_t$  is assumed and a pressure distribution obtained iteratively so that at the mesh points in the tangent plane

$$h(x, y) = h_t \quad \forall (x, y) \text{ with } p(x, y) \geq 0$$

$$h(x, y) \geq h_t \quad \forall (x, y) \text{ with } p(x, y) = 0$$

This is obtained by modifying the current pressure distribution  $p(x, y)$  at each stage in the iteration using the formula

$$p_{\text{new}}(x, y) = \left\{ (1 - \beta) + \beta \left[ 2 - \frac{h(x, y)}{h_t} \right] \right\} p_{\text{old}}(x, y) \quad (2)$$

The target deflection is chosen to correspond to the distance of elastic approach for the elliptical contact having the same radii of relative curvature loaded to the required contact load. To start the process, the required

deflection at each point is used to form the first trial pressure distribution according to

$$p(x, y) = k[h_t - h_u(x, y)] \quad \text{where } h_t \geq h_u(x, y)$$

$$= 0 \quad \text{elsewhere}$$

with constant  $k$  chosen so that  $p(x, y)$  supports the required contact load.

The iterative process is found to be extremely robust and its accuracy has been verified by considering elliptical Hertzian contacts so that comparison can be made with the Hertzian solution. Progress of the iterative method towards its solution can be optimized by suitable choice of the overrelaxation parameter  $\beta$ , and a value of  $\beta = 2.2$  has been found to be effective for the current work. The load supported for a specified value of  $h_t$  is established in relatively few cycles using a coarse mesh. This information is used to adjust  $h_t$  so that the closely converged fine mesh solution obtained supports the required load. The initial pressure distribution always encloses the final contact area. The iterative scheme described above does not reduce the pressure at points just outside the contact area to zero rapidly, as equation (2) will scale them by a factor only moderately less than unity in each iteration. The process is accelerated considerably by reducing such pressures by 15 per cent in each iteration once the contact shape has become established. A further advantage of this simple method is that it is able to deal with rough surface contacts quite easily, and difficulties associated with potential lack of connectivity of the pressurized regions do not impact on progress to the solution.

A problem encountered with the numerical data representing the two surfaces was that of precision. Although gap values to the precision produced by the numerical simulation were sufficient for conventional purposes such as transmission error analysis, etc., this led to a 'surface roughness' of sufficient magnitude to give sizeable corresponding ripples in the elastic and EHL pressure distributions in subsequent elastic and lubrication simulations. While it is recognized that all real engineering surfaces have such features, the initial aim of the work was to provide reference solutions to the ideally smooth surface case. The numerically obtained surfaces were therefore smoothed by fitting high-order polynomials to both worm and wheel surfaces. It was found that polynomials of up to order ten were sufficient to give a very good fit to the surfaces over the whole active part of the teeth. The undeformed gap between the surfaces was then obtained, for each of about 20 meshing positions, by subtraction of the two surface-fitting functions to give an analytical form for the clearance.

3 REYNOLDS EQUATION

Kinematic analysis is required to enable EHL simulations for the worm gear contacts. The velocities of interest are the components of velocity of the two surfaces in the common tangent plane relative to the instantaneous point of contact. This gives the distribution of hydrodynamic entraining, or rolling, velocity in the region of potential contact. The dominant effect is that of the sweeping velocity of the worm surface which gives entrainment in the direction of the streamlines shown in Fig. 2. This is a projection into the plane perpendicular to the worm axis containing the wheel axis and also shows the outer radius and throat radius of the worm, and the sides of the wheel. Surface velocities of the two components are obtained by conventional vector methods based on steady rotation of the worm and the wheel at angular velocities that are in the gear ratio. The instantaneous velocity of the point of contact is obtained by time differencing the contact positions established by the TCA. The entrainment conditions are extreme in that the wheel component makes relatively little contribution and the slide roll ratio is close to the value of 2 obtained in simple sliding. Consequently, very high shear rates, of order  $10^7 \text{ s}^{-1}$ , are imposed on the lubricant and a non-Newtonian rheological model is utilized. The situation is complicated by the systematic variation in the direction of sliding owing to the rotational motion of the worm, and this leads to new terms in the Reynolds equation when a non-Newtonian fluid model is used.

Consider a small quantity of fluid as shown in Fig. 3, where  $s$  is the local sliding direction in the tangent plane and  $r$  is the local rolling direction; i.e. if  $\mathbf{u}_s$  is the vector of the difference in surface velocities at the point  $(x, y)$ , then coordinate  $s$  is chosen as the direction of  $\mathbf{u}_s$ . The balance of pressure forces and shear stress forces on a small element of fluid leads to the equations

$$\frac{\partial \tau_s}{\partial z} = \frac{\partial p}{\partial s} \quad \text{and} \quad \frac{\partial \tau_r}{\partial z} = \frac{\partial p}{\partial r}$$

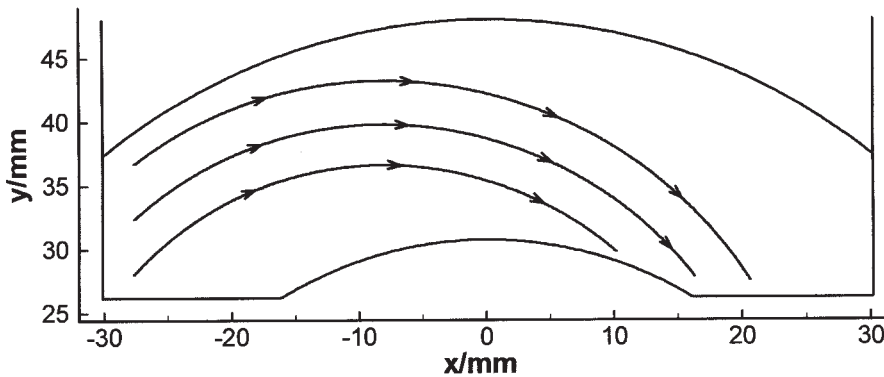


Fig. 2 Outline of the worm wheel tooth, showing the throat radius to accommodate the worm and the outer radius of the worm. Also shown are the entrainment velocity streamlines

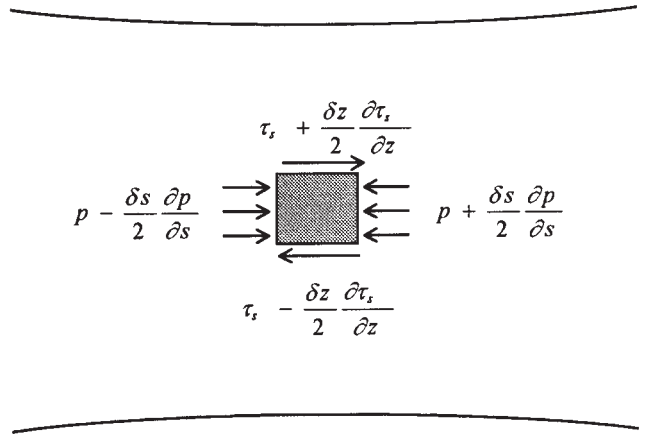


Fig. 3 Elemental volume of lubricating fluid between the contacting surfaces, showing forces acting in the  $s$  direction

and, integrating with respect to  $z$ , assuming that the pressure does not vary with  $z$ , the shear stress is

$$\tau_s(z) = \tau_{s_m} + z \frac{\partial p}{\partial s} \quad \text{and} \quad \tau_r(z) = \tau_{r_m} + z \frac{\partial p}{\partial r} \quad (3)$$

where  $\tau_{s_m}$  and  $\tau_{r_m}$  are the mid-plane ( $z = 0$ ) shear stress components.

The non-Newtonian formulation links shear strain rate with shear stress according to

$$\frac{\partial u}{\partial z} = F(\tau) \quad (4)$$

in a one-dimensional situation, and  $F(\tau)$  is the non-Newtonian function taken as either

$$F(\tau) = -\frac{\tau_L}{\eta} \ln\left(1 - \frac{\tau}{\tau_L}\right) \quad (5)$$

or

$$F(\tau) = \frac{\tau_0}{\eta} \sinh\left(\frac{\tau}{\tau_0}\right) \left\{ \frac{\tau_L^{2\nu}}{\tau_L^{2\nu} - \tau^{2\nu}} \right\} \quad (6)$$

Equation (5) is the model proposed by Bair and Winer [13], and equation (6) is an adaptation of the Eyring model proposed by Johnson and Tevarwerk [14] where the curly bracket has been added to allow limiting shear stress behaviour to be added to the Eyring behaviour. The parameter  $\nu$  is taken as unity but can be varied in numerical experiments to control the rate at which the shear stress approaches its limiting value  $\tau_L$  as discussed in Sharif *et al.* [15].

In two-dimensional flow situations the shear stress-strain rate relation of equation (4) becomes

$$\frac{\partial u}{\partial z} = \frac{\tau_s}{\tau_e} F(\tau_e), \quad \frac{\partial v}{\partial z} = \frac{\tau_r}{\tau_e} F(\tau_e) \quad (7)$$

where  $\tau_e = \sqrt{\tau_s^2 + \tau_r^2}$ .

These equations can be integrated across the thickness of the film to give the difference between the velocity components at the two solid boundaries. Thus

$$0 = -u_s + \int_{-h/2}^{h/2} \frac{\tau_s}{\tau_e} F(\tau_e) dz \quad (8)$$

$$0 = \int_{-h/2}^{h/2} \frac{\tau_r}{\tau_e} F(\tau_e) dz \quad (9)$$

are the kinematic conditions to be satisfied by the lubricant at each point in the contact. The shear stress components  $\tau_s$  and  $\tau_r$  are given by equations (3), and so equations (8) and (9) determine the values of the mid-plane shear stress components  $\tau_{sm}$  and  $\tau_{rm}$ , and thus the shear stress developed at each point in the fluid. In the numerical method, equations (8) and (9) are solved by a simple Newton method. The integrals are obtained by quadrature, as are those of the derivatives of the equations with respect to  $\tau_{sm}$  and  $\tau_{rm}$  that are required. When one of the limiting shear stress forms is used, care is required during the iterative solution of the equations at any mesh point. The iteration is started from a point  $(\tau_{sm}, \tau_{rm})$  in the plane illustrated in Fig. 4. Equations (3)

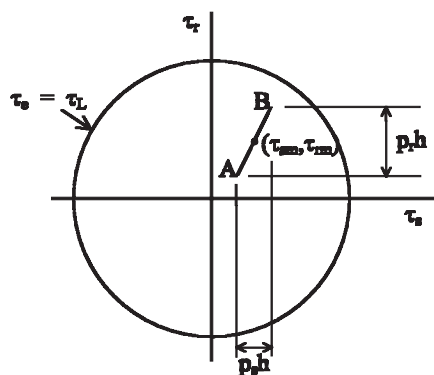


**Fig. 4** Vector AB, showing the variation in the shear stress over the thickness of the film in the shear stress plane. A and B are surface shear stress conditions

ensure that all points within the thickness of the film at the mesh point are represented by a straight line, or vector, in this figure, with  $(\tau_{sm}, \tau_{rm})$  at its centre. The most extreme value of  $\tau_e$  thus occurs at one or other of the surfaces. The initial iterative point is located within the limiting shear stress circle so that the most extreme  $\tau_e$  is less than  $0.95\tau_L$ . If, during subsequent iterations, the most extreme  $\tau_e$  value would breach the  $\tau_e = \tau_L$  circle, the change is limited to 20 per cent of the change that would correspond to the extreme value of  $\tau_e$  becoming exactly  $\tau_L$ , so that the limiting shear condition is approached in a series of diminishing steps. If the extreme  $\tau_e$  value then reaches  $0.995\tau_L$ , the calculation is halted with slip at that surface and no slip at the other surface. This situation has only been found to occur in solutions when the Bair and Winer [13] formulation of equation (5) is adopted. Whether or not the liquid is actually slipping at the surface or has an extremely high shear rate near the surface is really a matter of the precise form of  $F(\tau)$  as limiting shear conditions are approached, and is not felt to be a significant issue in the context of the work reported here. A singular integral treatment could easily be adopted for clarification should this prove to be of engineering interest.

The mass flowrate in each of the axis directions is given by

$$Q_s = \int_{-h/2}^{h/2} \rho u(z) dz, \quad Q_r = \int_{-h/2}^{h/2} \rho v(z) dz$$

which, provided  $\rho$  is taken not to vary across the film, can be rewritten following Greenwood [16] as

$$Q_s = [\rho uz]_{-h/2}^{h/2} - \int_{-h/2}^{h/2} \rho z \frac{\partial u}{\partial z} dz$$

and

$$Q_r = [\rho vz]_{-h/2}^{h/2} - \int_{-h/2}^{h/2} \rho z \frac{\partial v}{\partial z} dz$$

so that

$$Q_s = \rho \bar{u}h - \int_{-h/2}^{h/2} \rho z \frac{\tau_s}{\tau_e} F(\tau_e) dz \quad (10)$$

$$Q_r = \rho \bar{v}h - \int_{-h/2}^{h/2} \rho z \frac{\tau_r}{\tau_e} F(\tau_e) dz \quad (11)$$

It is found [17] that, provided the flow expressions are formulated in the direction of sliding and non-sliding, the integral term in each of these expressions is broadly proportional to the pressure gradient in that particular direction so that it is possible to write

$$Q_s = \rho \bar{u}h - D \frac{\partial p}{\partial s} \quad \text{and} \quad Q_r = \rho \bar{v}h - C \frac{\partial p}{\partial r} \quad (12)$$

where  $D(h, p, \partial p/\partial s, \partial p/\partial r)$  and  $C(h, p, \partial p/\partial s, \partial p/\partial r)$  are given by

$$D = \left(\frac{\partial p}{\partial s}\right)^{-1} \int_{-h/2}^{h/2} \rho z \frac{\tau_s}{\tau_e} F(\tau_e) dz \tag{13}$$

and

$$C = \left(\frac{\partial p}{\partial r}\right)^{-1} \int_{-h/2}^{h/2} \rho z \frac{\tau_r}{\tau_e} F(\tau_e) dz \tag{14}$$

The flow factors  $C$  and  $D$  in equations (13) and (14) are then smoothly varying functions over the contact area and correspond to the term  $(\rho h^3)/(12\eta)$  seen in the familiar Newtonian form of the Reynolds equation. In non-Newtonian situations, factors  $C$  and  $D$  have different values, and recognition of this factor distinguishes the current approach from the work of Kim and Sadeghi [18]. Formulation in arbitrary directions not corresponding to the sliding and non-sliding directions is mathematically possible, but the resulting flow factors are not smoothly varying functions and do not lend themselves to the linearization solution scheme described below. It would seem that the effective viscosity in the sliding direction is intrinsically different to that in the non-sliding direction and that this needs to be recognized in considering general kinematic conditions. Greenwood [16] has also pointed out this feature based on analytical considerations. Care is necessary in evaluating these flow factors when the pressure gradients tend to or become zero, where a limiting process is required.

The situation is further complicated if the cross-film temperature dependence is included in the viscosity model, as the flow corresponding to a zero pressure gradient in the sliding direction cannot then be taken as  $\rho \hat{u} h$  since a further contribution proportional to the sliding velocity occurs. In these circumstances, when  $\tau_{s_m}$  and  $\tau_{r_m}$  are obtained by solving equations (8) and (9) and the flow terms are established numerically as

$$Q_s(p_s, p_r, h, \eta, \tau_{s_m}, \tau_{r_m}) \quad \text{and} \quad Q_r(p_s, p_r, h, \eta, \tau_{s_m}, \tau_{r_m}) \tag{15}$$

with  $\eta = \eta(z)$ , corresponding expressions for  $Q_s$  and  $Q_r$ , with  $p_s$  and  $p_r$  set to zero respectively, are also evaluated. This gives the effective entrainment velocities  $\hat{u}$  and  $\hat{v}$ , so that the Couette flow components are

$$\rho \hat{u} h = Q_s(0, p_r, h, \eta, \tau_{s_m}, \tau_{r_m})$$

and

$$\rho \hat{v} h = Q_r(p_s, 0, h, \eta, \tau_{s_m}, \tau_{r_m}) \tag{16}$$

The flow factors are then established from

$$D = -\left(\frac{\partial p}{\partial s}\right)^{-1} [Q_s(p_s, p_r, h, \eta, \tau_{s_m}, \tau_{r_m}) - Q_s(0, p_r, h, \eta, \tau_{s_m}, \tau_{r_m})] \tag{13a}$$

and

$$C = -\left(\frac{\partial p}{\partial r}\right)^{-1} [Q_r(p_s, p_r, h, \eta, \tau_{s_m}, \tau_{r_m}) - Q_r(p_s, 0, h, \eta, \tau_{s_m}, \tau_{r_m})] \tag{14a}$$

Equations (12) may then be taken as the general flow expressions, with  $\bar{u}$  and  $\bar{v}$  replaced by  $\hat{u}$  and  $\hat{v}$  respectively.

To obtain the Reynolds equation, the local sliding axis set  $Osr$ , inclined at an angle  $\phi$  to the global axis set  $Oxy$ , is considered as shown in Fig. 5. For a general kinematic situation,  $\phi$  will vary over the tangent plane and  $\phi$  constant will be a special case.

The angle  $\phi$  is determined from the equation

$$0 = -(U_2 - U_1) \sin \phi + (V_2 - V_1) \cos \phi$$

and the sliding speed is

$$u_s = (U_2 - U_1) \cos \phi + (V_2 - V_1) \sin \phi$$

The pressure gradients are related by

$$\frac{\partial p}{\partial s} = \cos \phi \frac{\partial p}{\partial x} + \sin \phi \frac{\partial p}{\partial y}$$

$$\frac{\partial p}{\partial r} = -\sin \phi \frac{\partial p}{\partial x} + \cos \phi \frac{\partial p}{\partial y}$$

which enables flow factors  $C$  and  $D$  to be evaluated numerically at any point in the tangent plane.

The flow expressions of equation (12)

$$Q_s = \rho \hat{u} h - D \frac{\partial p}{\partial s} \quad \text{and} \quad Q_r = \rho \hat{v} h - C \frac{\partial p}{\partial r}$$

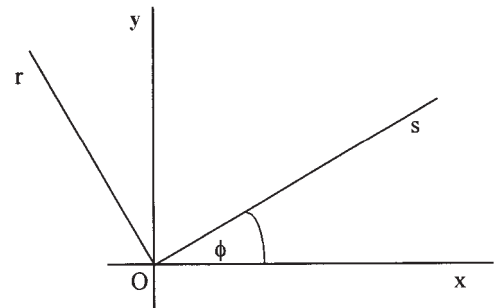


Fig. 5 Local sliding and non-sliding directions  $Osr$ , showing global axes  $Oxy$

can then be written in terms of the global gradients as

$$Q_s = \rho \hat{u}h - D \left( \cos \phi \frac{\partial p}{\partial x} + \sin \phi \frac{\partial p}{\partial y} \right)$$

and

$$Q_r = \rho \hat{v}h - C \left( -\sin \phi \frac{\partial p}{\partial x} + \cos \phi \frac{\partial p}{\partial y} \right)$$

and used to form expressions for the flow in the global axis directions:

$$Q_x = \left[ \rho \hat{u}h - D \left( \cos \phi \frac{\partial p}{\partial x} + \sin \phi \frac{\partial p}{\partial y} \right) \right] \cos \phi - \left[ \rho \hat{v}h - C \left( -\sin \phi \frac{\partial p}{\partial x} + \cos \phi \frac{\partial p}{\partial y} \right) \right] \sin \phi$$

$$Q_y = \left[ \rho \hat{u}h - D \left( \cos \phi \frac{\partial p}{\partial x} + \sin \phi \frac{\partial p}{\partial y} \right) \right] \sin \phi + \left[ \rho \hat{v}h - C \left( -\sin \phi \frac{\partial p}{\partial x} + \cos \phi \frac{\partial p}{\partial y} \right) \right] \cos \phi$$

i.e.

$$Q_x = \rho \hat{U}h - (D \cos^2 \phi + C \sin^2 \phi) \frac{\partial p}{\partial x} - (D - C) \sin \phi \cos \phi \frac{\partial p}{\partial y}$$

$$Q_y = \rho \hat{V}h - (D - C) \sin \phi \cos \phi \frac{\partial p}{\partial x} - (D \sin^2 \phi + C \cos^2 \phi) \frac{\partial p}{\partial y}$$

which since the flow balance is given by

$$\frac{\partial Q_x}{\partial x} + \frac{\partial Q_y}{\partial y} = 0$$

leads to a 'Reynolds' equation as follows:

$$\begin{aligned} & \frac{\partial}{\partial x} \left[ (D \cos^2 \phi + C \sin^2 \phi) \frac{\partial p}{\partial x} \right] \\ & + \frac{\partial}{\partial y} \left[ (D \sin^2 \phi + C \cos^2 \phi) \frac{\partial p}{\partial y} \right] \\ & + \frac{\partial}{\partial x} \left[ (D - C) \cos \phi \sin \phi \frac{\partial p}{\partial y} \right] \\ & + \frac{\partial}{\partial y} \left[ (D - C) \cos \phi \sin \phi \frac{\partial p}{\partial x} \right] \\ & = \frac{\partial}{\partial x} (\rho \hat{U}h) + \frac{\partial}{\partial y} (\rho \hat{V}h) \end{aligned} \quad (17)$$

This reduces to the expected form

$$\frac{\partial}{\partial x} \left( D \frac{\partial p}{\partial x} \right) + \frac{\partial}{\partial y} \left( C \frac{\partial p}{\partial y} \right) = \frac{\partial}{\partial x} (\rho \hat{U}h) + \frac{\partial}{\partial y} (\rho \hat{V}h)$$

for the special case  $\phi = 0$ , where the sliding direction is in the  $x$  direction at all points, and also for Newtonian situations where  $C \equiv D$ .

#### 4 ELASTOHYDRODYNAMIC EQUATIONS

The equations that describe the hydrodynamic aspect of the EHL solution are thus equation (17) with the flow factors  $D(h, p, \partial p/\partial s, \partial p/\partial r)$  and  $C(h, p, \partial p/\partial s, \partial p/\partial r)$  obtained from equations (13) and (14), or (13a) and (14a). The elastic deflection is given by the deflection of contacting semi-infinite bodies so that the film thickness is given by equation (1) in the form

$$h(x, y) = h_0 + h_u(x, y) + \frac{2}{\pi E'} \iint_A \frac{p(x', y')}{\sqrt{(x' - x)^2 + (y' - y)^2}} dx' dy'$$

with the energy equation given by

$$\begin{aligned} \rho c \left( U \frac{\partial \theta}{\partial x} + V \frac{\partial \theta}{\partial y} \right) &= \tau_x \frac{\partial U}{\partial z} + \tau_y \frac{\partial V}{\partial z} + \varepsilon \theta \left( U \frac{\partial p}{\partial x} + V \frac{\partial p}{\partial y} \right) \\ &+ \frac{\partial}{\partial x} \left( k \frac{\partial \theta}{\partial x} \right) + \frac{\partial}{\partial y} \left( k \frac{\partial \theta}{\partial y} \right) \\ &+ k \left( \frac{\partial^2 \theta}{\partial z^2} \right) \end{aligned} \quad (18)$$

The boundary conditions for this equation are given by the surface temperatures of the worm and wheel tooth components. These are obtained using a simple one-dimensional (linear heat flow) conduction model so that the surface temperatures are given by integrals of the form

$$\theta_S = \theta_{\text{ref}} + \frac{1}{\sqrt{\pi k \rho c}} \int_0^t \frac{q d\lambda}{\sqrt{t - \lambda}} \quad (19)$$

The lubricant viscosity is taken to be given by the formula of Roelands [19]

$$\begin{aligned} \eta &= \eta_0 \exp \left\{ [\ln(\eta_0) + 9.67] \right. \\ &\quad \left. \times \left[ (1 + 5.1 \times 10^{-9} p)^Z \left( \frac{\theta_0 - 138}{\theta - 138} \right)^{S_0} - 1 \right] \right\} \end{aligned} \quad (20)$$

## 5 NUMERICAL SOLUTION

These equations are solved numerically using a finite difference method. The combination of a non-Newtonian formulation and load cases where the maximum contact pressure is limited by the elastic limit of bronze leads to a relatively soft EHL problem, and a simple forward iterative method has been used to obtain solutions. The model is not limited to such lightly loaded cases and has also been applied in isothermal form to extremely heavily loaded point contacts, as encountered in traction drives, and outlined by Holmes [20] using a new fully coupled point contact solution approach based on the differential deflection method of Evans and Hughes [21].

In the present work, thermal equation (18) is solved by rearranging the terms to the form

$$\begin{aligned} & \frac{\partial}{\partial x} \left( k \frac{\partial \theta}{\partial x} \right) + \frac{\partial}{\partial y} \left( k \frac{\partial \theta}{\partial y} \right) + k \frac{\partial^2 \theta}{\partial z^2} \\ & - \rho c \left( U \frac{\partial \theta}{\partial x} + V \frac{\partial \theta}{\partial y} \right) + \varepsilon \left( U \frac{\partial p}{\partial x} + V \frac{\partial p}{\partial y} \right) \theta \\ & = -\tau_x \frac{\partial U}{\partial z} - \tau_y \frac{\partial V}{\partial z} \end{aligned} \quad (21)$$

In solving equation (21) numerically, the film is partitioned into  $n_f$  cross-film node points. The right-hand side and the velocity and pressure gradient dependent coefficients in the terms in  $\theta$  and its derivatives are evaluated at each cross-film node point using the outer loop values of these parameters. The conductive derivative terms are expressed in central difference form, and backward or forward differences are used for the convective terms according to the sign of the fluid velocity components at each mesh point and level. The current values of the surface temperatures are regarded as boundary conditions, and thus there are  $n_f - 2$  equations at the  $n_f - 2$  cross-film node point temperatures at each  $(x, y)$  position. The temperature values at other  $(x, y)$  positions are taken as their current approximation (outer loop) values. Thus, at each  $(x, y)$  position there are  $n_f - 2$  equations in  $n_f - 2$  unknowns. These equations are solved with a tridiagonal solver to produce a new cross-film temperature field. Temperature value boundary conditions are imposed at the boundary at all  $z$  values where oil is flowing into the computing region. The equation is not solved on the boundary but at points adjacent to the boundary. At the boundary positions for  $z$  values where the oil is flowing out of the computing region, the treatment of the convective terms ensures that no boundary condition is imposed through these terms. The second-order conductive terms require a boundary condition to be imposed, and for outflowing lubricant this is achieved by specifying that there is no conductive heat flux out of the computing region.

To complete the temperature calculation, the temperature gradient,  $\partial\theta/\partial z$ , is evaluated at the solid liquid interfaces and used to give the term  $q$  so that each of the surface temperatures may be recalculated from equation (19). For each point on the surface the integral of equation (19) is evaluated taking account of the locus of the surface point in reaching its current position so that the time integral is converted into a spatial integral over a curved path determined by the motion of the component relative to the instantaneous contact point. The reference surface temperature,  $\theta_{\text{ref}}$ , of each body is specified independently to be the bulk temperature value for the component. In this way, each of the two solid bodies is assumed to enter the computing region at the specified (possibly different) bulk temperature for that component, and thus the thermal model allows the appropriate surface flash temperatures to be calculated. In practice, the bulk temperature of the steel worm may well be 15 K higher than that of the bronze wheel.

This sequence of thermal calculations is carried out once for each cycle of the EHL convergence process. The interface temperature gradients and cross-film temperature distribution are found to stabilize quickly and converge reliably. The overall solution is obtained when the pressure, film thickness and temperature fields converge, with the constant  $h_0$  in the film thickness equation adjusted to obtain the required load.

## 6 RESULTS OF A TYPICAL CALCULATION

The results of the analysis methods for one particular worm gear combination are presented at a point midway through the meshing cycle. The worm design under consideration is a three-start 59:3 ratio set with the design variables given in Table 1. The operating conditions and elastic, rheological and thermal properties used are given in Table 2. Where properties are taken to be temperature or pressure dependent, the expressions used are given in the Appendix. The lubricant modelled is a 460 ISO viscosity-grade polyglycol synthetic gear oil used for worm gears and in an associated experimental project. Lubricant parameter  $Z$  in equation (20) was determined by measuring film thickness in an optical interference rig in pure rolling conditions over a range of temperatures and adjusting  $Z$  in the numerical model to achieve the same film/speed characteristic;  $S_0$  was determined by measuring the viscosity as a function of temperature. Guidance in specifying these and other lubricant parameters and their possible dependence on pressure or temperature was taken from Larsson *et al.* [22]. The component velocities are such that the Peclet number  $[U\rho c/(2k)]$  for the worm is approximately 1000, and that for the wheel is approximately 5, so that the assumption of linear heat flow leading to equation (19) is justified. A more detailed thermal analysis that also includes conduction in the solids parallel to the film

**Table 1** Worm/wheel design parameters

Number of worm threads	3
Worm tip radius (mm)	48.01
Worm root radius (mm)	29.03
Worm base radius (mm)	26.23
Worm axial pitch (mm)	28.73
Worm lead (mm)	86.18
Worm base lead angle (deg)	27.61
Number of wheel teeth	59
Wheel face width (mm)	60.33
Wheel tip radius (mm)	278.61
Wheel throat radius (mm)	274.03
Hob tip radius (mm)	51.63
Hob root radius (mm)	31.58
Hob base radius (mm)	26.48
Hob lead (mm)	85.97
Hob axial pitch (mm)	28.66
Hob base lead angle (deg)	27.33
Hob/wheel centre distance (mm)	305.62
Worm/wheel centre distance (mm)	304.8

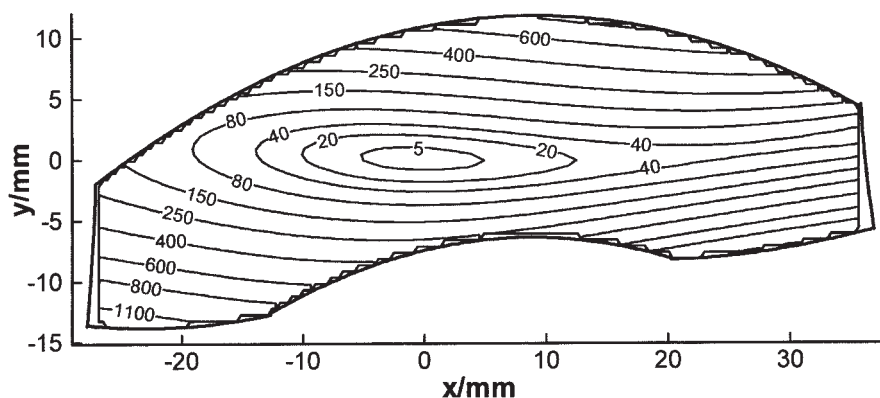
**Table 2** Worm/wheel operating conditions, material properties and lubricant properties

<i>Operating conditions</i>		
Worm input speed ( $r/min$ )	1500	
Assumed tooth normal load (N)	14000	
Maximum contact pressure (MPa)	540	
<i>Material properties</i>		
	Worm	Wheel
Modulus of elasticity (GPa)	207	120
Poisson's ratio	0.3	0.35
Density ( $kg/m^3$ )	7900	8800
Thermal conductivity (W/m K)	47	52
Specific heat (J/kg K)	477	420
<i>Lubricant properties</i>		
Inlet temperature $\theta_0$ ( $^{\circ}C$ )	60	
Inlet viscosity $\eta_0$ (Pa s)	0.227	
Inlet density $\rho_0$ ( $kg/m^3$ )	1025	
Lubricant parameter $Z$	0.227	
Lubricant parameter $S_0$	0.782	
Equivalent pressure viscosity coefficient at $60^{\circ}C$ ( $GPa^{-1}$ )	9.5	
Eyring shear stress $\tau_0$ (MPa)	3	
Limiting shear stress $\tau_L$ (MPa)	100	
Thermal expansivity $\varepsilon_0$ ( $K^{-1}$ )	$7.1 \times 10^{-4}$	
Thermal conductivity $k_0$ (W/m K)	0.148	
Specific heat $c_0$ (J/kg K)	1844	

confirms that the use of equation (19) has no significant effect on the results presented. Comparisons of results such as those shown in this paper over entire meshing sequences and between different single and multistart ZI designs are presented in references [23] and [24].

Figure 6 illustrates the undeformed contact contours shown against the outline of the wheel tooth in the tangential plane. The contours can be seen to be asymmetric and have aspect ratios of approximately 6. (The stepped nature of the contours at some of the boundaries is a consequence of specifying large values of the gap outside the region where both teeth are present. All contours that reach tooth boundaries are open contours.) Figure 7 shows the dry contact solution for the same case at a load of 14 kN which gives a maximum contact stress of 540 MPa, corresponding to a typical limit of allowable contact stress for the bronze component. The degree of asymmetry apparent in the undeformed contours is somewhat reduced in the deformed contours and the aspect ratio of the contact area is approximately 10. The radii of relative curvature at the contact point are 3.046 m and 95.4 mm so that Hertzian contact theory would predict an elliptic contact of 21.5 mm by 2.3 mm. The contact illustrated in Fig. 7 has major and minor dimensions of 23.2 and 2.4 mm respectively, so that it is 8 per cent longer and 3 per cent wider than the Hertz contact. The pressure distribution corresponding to the dry contact of Fig. 7 is illustrated in Fig. 8.

The inclusion of lubricant in the contact and subsequent EHL analysis gives rise to the results illustrated in Figs 9 to 14. Figure 9 shows the EHL pressure distribution which can be seen to differ from the dry contact case, although it is clear that the contact is heavily loaded in EHL terms with very little effective pressure distribution outside the dry contact area. This is confirmed by the pressure contours shown in Fig. 10 together with the dry contact area. It is seen that the 100 MPa contour is just inside the dry contact area and that little significant lubricant pressure is developed outside the contact area, confirming the heavily loaded nature of the elastohydrodynamic contact. An unexpected shoulder feature is seen in the pressure distribution to the top right of Fig. 9. There is no corresponding

**Fig. 6** Undeformed contact contours ( $\mu m$ ) obtained by polynomial fitting of TCA data

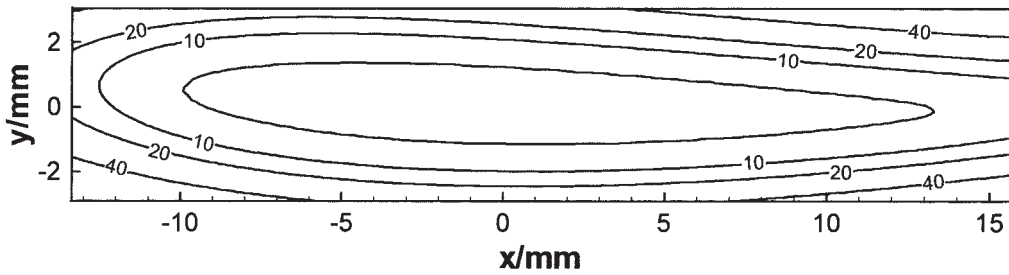


Fig. 7 Contact area and surrounding contours ( $\mu\text{m}$ ) obtained using dry elastic contact analysis

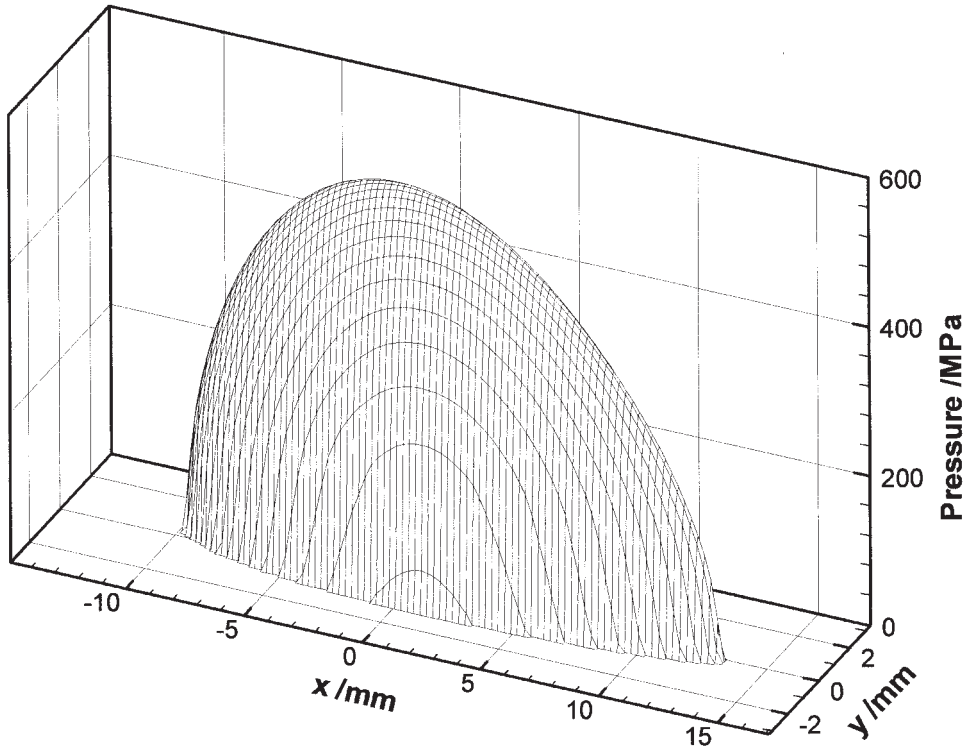


Fig. 8 Isometric view of the pressure distribution obtained from dry contact analysis

feature in the dry contact pressure distribution of Fig. 8, and the location of the intersection of this pressure shoulder with the main pressure distribution is seen to correspond to the upper of two thin film side lobes seen in the film thickness contours illustrated in Fig. 11. Two thin film side lobes are to be expected in longitudinally entrained elliptical contacts, but in this case there is considerable asymmetry. The upper thin film area is larger and has thinner film values than the lower area. It is also seen effectively to cross the contact area which is quite unexpected. The upper thin film area might be expected to have thicker films than the lower one owing to the higher values of entraining velocity at the greater worm radius. The explanation for this unexpected feature lies in the particular kinematic conditions that are found in worm gears. Figure 2 showed the streamlines for the entrainment velocity produced by the motion of

the two gear components relative to the contact point. Figure 12 shows the dry contact area of Fig. 7 to which two particular entrainment streamlines have been added, those that pass through the two positions A and B indicated in the figure. Points A and B are the positions where the entrainment streamline is tangential to the dry contact area (with A at the greater distance from the worm axis than B). Point C is the extreme position on the dry contact boundary for entrainment into the contact from the bottom left of the figure, and point D is the extreme position for entrainment over the upper edge of the dry contact area. It is seen from comparison with Fig. 11 that the streamlines through A and C enclose the elongated thin film area which is partly caused by a form of self-starvation of the contact. There are two sections of the dry contact boundary over which lubricant is effectively entrained into the contact, peri-

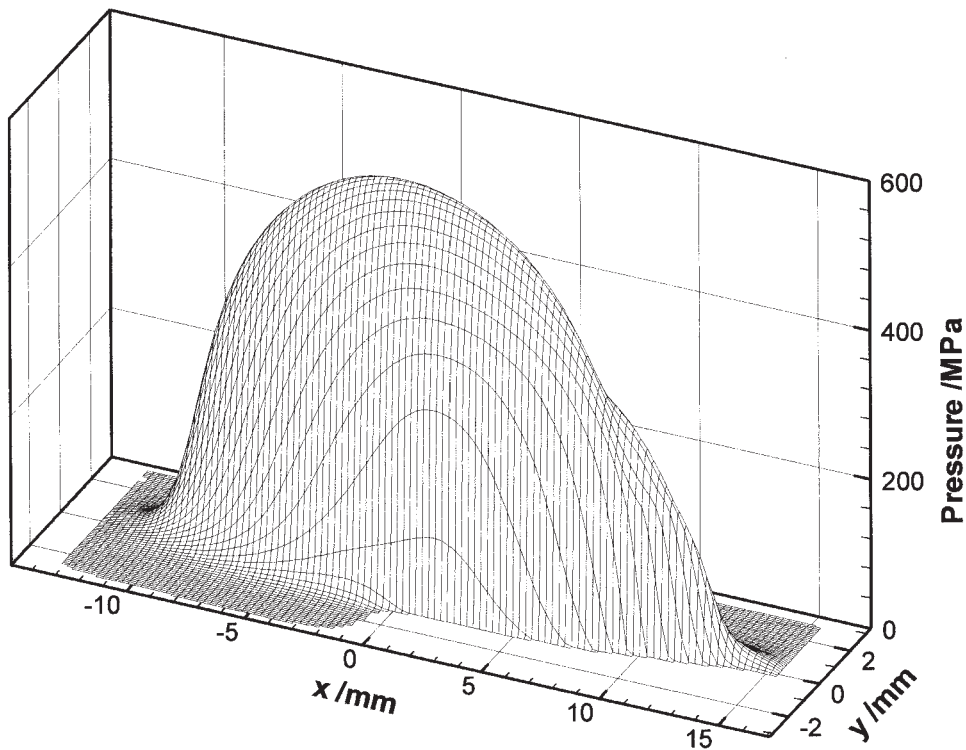


Fig. 9 Isometric view of the pressure distribution obtained from EHL analysis

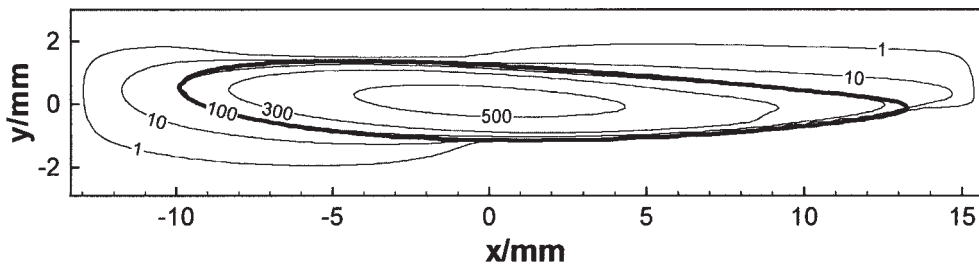


Fig. 10 Pressure contours (MPa). The heavy curve indicates the dry contact area

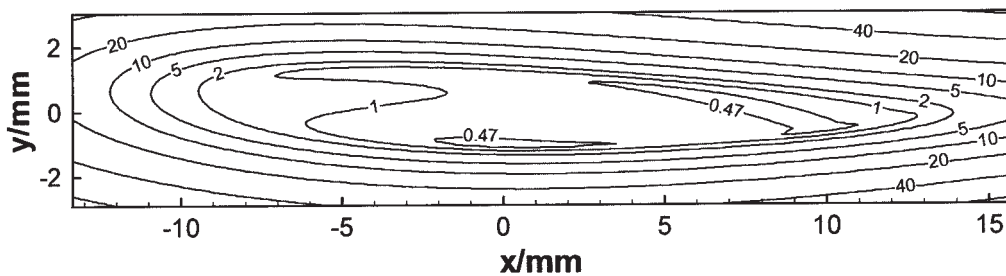


Fig. 11 Film thickness contours ( $\mu\text{m}$ ) obtained from EHL analysis

meter sections BC and AD. The thin film area can only be supplied with oil from an area (between the streamlines through C and A) that contains oil that has exited the EHL contact area upstream. This oil supply is limited, and the thin films observed are the result. Indeed, it

would seem that this upper thin film area is an inherent film-forming weakness for relatively high-conformity worm contacts. The existence or otherwise of these key positions is a kinematic consequence of the shape of the dry contact area and its orientation to the entrainment

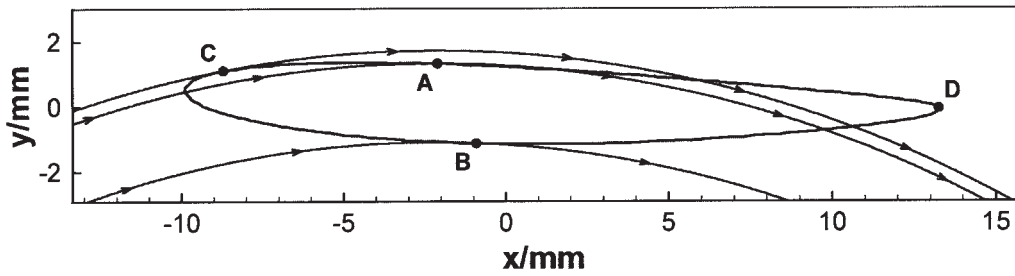


Fig. 12 Dry contact area of Fig. 7 with the key entrainment velocity superimposed

streamlines. These factors are discussed for a range of worm designs in Part 2 [23].

Figure 13 shows the temperature contours calculated for the two components and for the oil at the mid-plane ( $z = 0$ ) position. The worm surface sweeps from left to right relative to the contact, and Fig. 13a shows that there is a build-up of temperature towards the exit, as might be expected with a maximum calculated worm surface temperature of  $108^\circ\text{C}$ . The wheel surface moves much more slowly relative to the instantaneous point of contact and in a direction which is nominally perpendicular to that of the worm. As viewed in Fig. 13b, it moves

downwards as it passes through the contact, receiving heat input, and this results in a maximum temperature of  $106^\circ\text{C}$  as the surface exits the corresponding dry contact area at the bottom of the figure. The predominant heat transfer mechanism within the oil in the contact area is conduction perpendicular to the surfaces, as has been exploited in the solution technique described in Section 6. For the oil to transport heat by conduction, it generally acquires a temperature that is higher than both surface temperatures, but where the surface temperatures are considerably different the temperature of the oil may be found not to exceed that of the hottest surface so that at

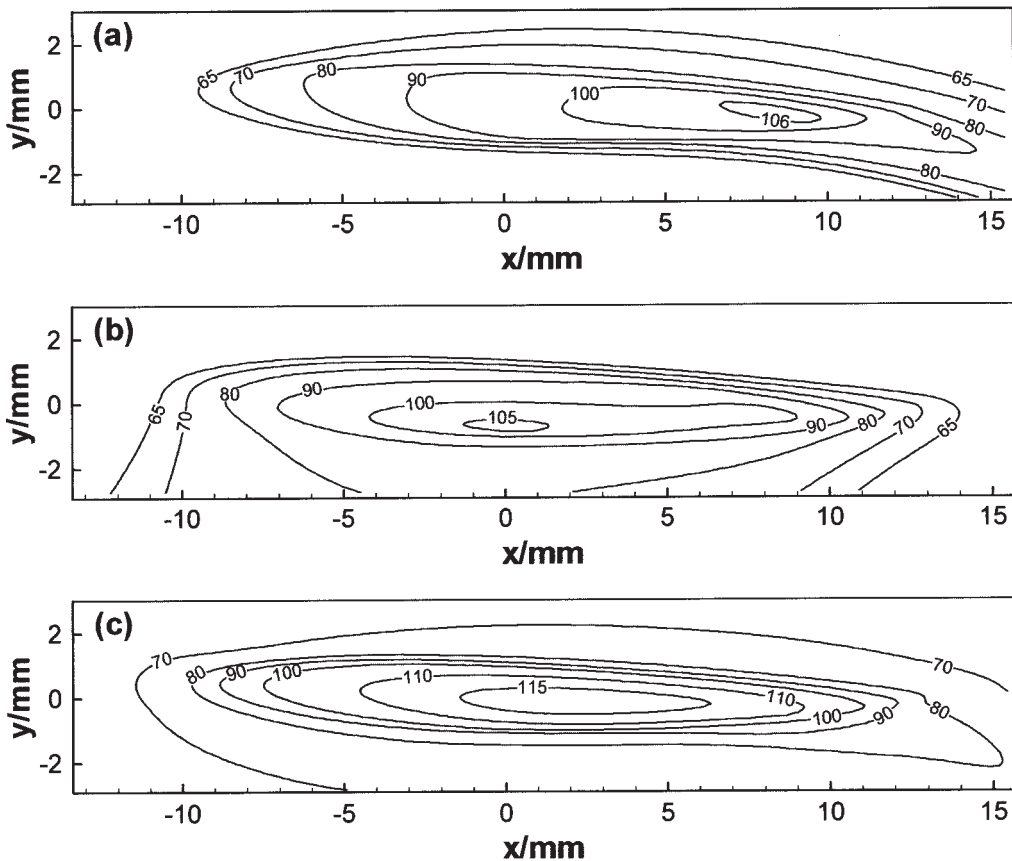


Fig. 13 Temperature contours ( $^\circ\text{C}$ ) obtained from EHL analysis: (a) worm surface temperature; (b) wheel tooth surface temperature; (c) oil mid-plane temperature

those locations conduction is principally into the colder of the two surfaces. The maximum mid-plane oil temperature shown in Fig. 13c is seen to occur at a location between the maximum temperature of the worm and that of the wheel. The value is  $117^{\circ}\text{C}$  which is a temperature rise of  $57^{\circ}\text{C}$ . The wheel surface temperature tends to build up towards the lower part of the contact as shown, and an important consequence of this behaviour is that heat generated by sliding in the contact is effectively solid-convected back into the primary hydrodynamic inlet of the contact by the motion of the wheel tooth, where it contributes to film thinning by reducing the controlling inlet viscosity. This behaviour is not generally seen in EHL contacts with linear entrainment, in which the inlet is virtually unaffected by transient heating in the main load-bearing region. Figure 14 shows an isometric projection of the mid-plane oil temperature (whose contours are shown in Fig. 13c) and clearly illustrates the way in which oil leaves the dry contact area at the bottom right with elevated temperatures. It is seen that no significant inlet shear heating is predicted as there is no temperature rise in the main inlet region where oil is fed into inlet section AC.

## 7 CONCLUSIONS

Elastic contact simulation reveals the area of dry elastic contact between worm gear teeth. Some significant departure from the Hertzian shape is seen.

A full elastic, non-Newtonian, thermal EHL model has been formulated for analysis of worm gear tooth

contacts. The non-Newtonian model has been developed to be applicable to general kinematic conditions, leading to a new form of the Reynolds equation incorporating cross-derivative pressure terms and flow factors in the local rolling and sliding directions. The spin component of relative velocity between the teeth necessitates the use of this form of the Reynolds equation, and the high degree of sliding requires full consideration of shear thinning, limiting shear stress and thermal effects. Application of the methods to a typical worm contact indicates that the conditions are heavily loaded in the elastohydrodynamic sense. Some subtle features of lubrication under these conditions are revealed. The EHL contact can effectively become separated into two parts, with the boundary between them a narrow region of poor film formation. Significant heating of the surfaces on account of lubricant shear takes place, and unfavourable solid convection of heat into the primary inlet to the contact reduces the effective viscosity of the lubricant in this crucial zone.

## ACKNOWLEDGEMENTS

The authors acknowledge the assistance of Dr J. Hu and Mr A. Pennell of Newcastle University in providing the geometry analysis software used in this project and also for many helpful discussions. The authors are also grateful for the financial support provided by EPSRC grant GR/L 69824 and for further financial support by the British Gear Association (<http://www.bga.org.uk>).

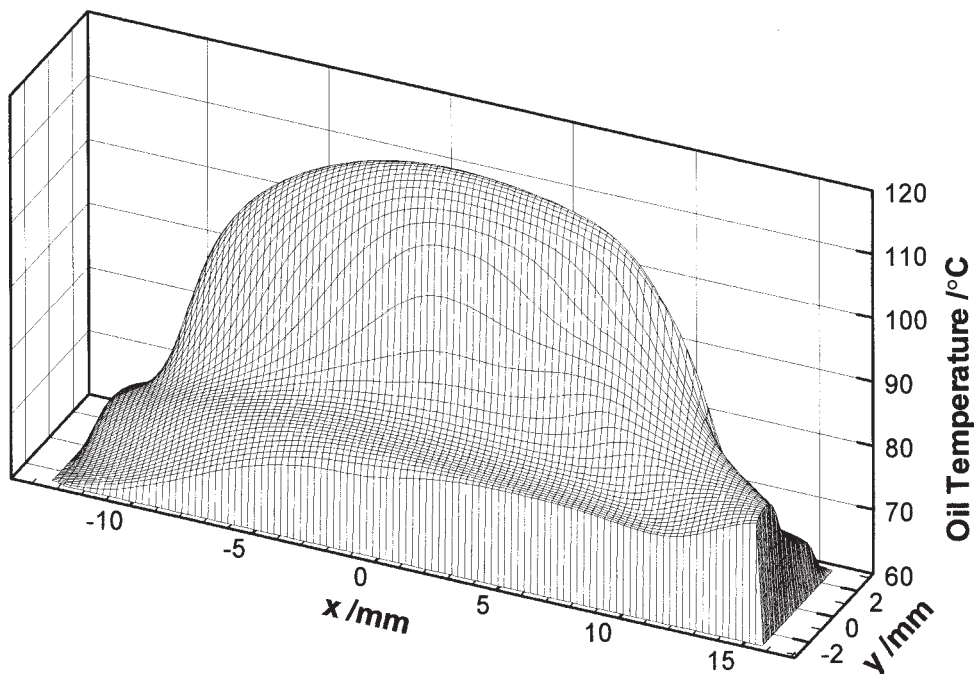


Fig. 14 Isometric view of the oil mid-plane temperature distribution from EHL analysis

## REFERENCES

- 1 Britton, R. D., Elcoate, C. D., Alanou, M. P., Evans, H. P. and Snidle, R. W. Effect of surface finish on gear tooth friction. *Trans. ASME, J. Tribology*, 2000, **122**, 354–360.
- 2 Litvin, F. L. and Kin, V. Computerised simulation of meshing and bearing contact for single-enveloping worm-gear drives. *Trans. ASME, J. Mech. Des.*, 1992, **114**, 313–316.
- 3 Seol, I. H. and Litvin, F. L. Computerised design, generation and simulation of meshing and contact of modified involute, Klingelnberg and Flender type worm-gear drives. *Trans. ASME, J. Mech. Des.*, 1996, **118**, 551–555.
- 4 Fang, H. and Tsay, C. Mathematical model and bearing contacts of the ZK-type worm gear set cut by oversize hob cutters. *Mech. Mach. Theory*, 1996, **31**, 271–282.
- 5 Hu, J. The kinematic analysis and metrology of cylindrical worm gearing. PhD thesis, University of Newcastle upon Tyne, 1997.
- 6 Su, D., Yang, F. and Gentle, C. R. A new approach combining numerical analysis and three dimensional simulation for design of worm gearing with preferable localised tooth contact. In Proceedings of ASME Design Engineering Technical Conference, Atlanta, Georgia, 1998, pp. 1–9.
- 7 Bathgate, J. and Yates, F. The application of film thickness, flash temperature and surface fatigue criteria to worm gears. *ASLE Trans.*, 1970, **13**, 21–28.
- 8 Fuan, C., Chen, Z., Yuehai, S. and Jing, S. Lubrication basis theory of worm pair and temperature distribution on worm gear surface. *Chin. J. Mech. Engng*, 1998, **11**, 19–22.
- 9 Simon, V. Thermoelastohydrodynamic analysis of lubrication of worm gears. In Proceedings of JSLE International Tribology Conference, Tokyo, Japan, 1985, pp. 1147–1152.
- 10 Simon, V. EHD lubrication characteristics of a new type of ground cylindrical worm gearing. *Trans. ASME, J. Mech. Des.*, 1997, **119**, 101–107.
- 11 Kong, S. Contact, kinematics and film formation in worm gears. PhD thesis, University of Wales, 2001.
- 12 Snidle, R. W. and Evans, H. P. A simple method of elastic contact simulation. *Proc. Instn Mech. Engrs, Part J, Journal of Engineering Tribology*, 1994, **208**(J4), 291–293.
- 13 Bair, S. and Winer, W. O. A rheological model for elastohydrodynamic contacts based on primary laboratory data. *Trans. ASME, J. Lubric. Technol.*, 1979, **101**, 258–265.
- 14 Johnson, K. L. and Tevaarwerk, J. L. The shear behaviour of elastohydrodynamic oil films. *Proc. R. Soc. (Lond.) A*, 1977, **356**, 217.
- 15 Sharif, K. J., Morris, S. J., Evans, H. P. and Snidle, R. W. Comparison of non-Newtonian EHL models in high sliding applications. Paper presented at 27th Leeds–Lyon Symposium on Tribology, Lyon, 2000.
- 16 Greenwood, J. A. Two-dimensional flow of a non-Newtonian lubricant. *Proc. Instn Mech. Engrs, Part J, Journal of Engineering Tribology*, 2000, **214**(J1), 29–41.
- 17 Morris, S. J. Traction in elliptical point contacts. PhD thesis, University of Wales, 2000.
- 18 Kim, K. H. and Sadeghi, F. Non-Newtonian elastohydrodynamic lubrication of point contact. *Trans. ASME, J. Tribology*, 1991, **113**, 703–711.
- 19 Roelands, C. J. A. Correlation aspects of the viscosity–temperature–pressure relationship of lubricating oils. PhD thesis, Technical University Delft, The Netherlands, 1966 (V.R.B. Gronigen, The Netherlands).
- 20 Holmes, M. A fully coupled method for solving the Newtonian, steady state, isothermal elastohydrodynamic point contact problem. *Proc. South Wales Inst. Engrs*, 2000.
- 21 Evans, H. P. and Hughes, T. G. Evaluation of deflection in semi-infinite bodies by a differential method. *Proc. Instn Mech. Engrs, Part C, Journal of Mechanical Engineering Science*, 2000, **214**(C4), 563–584.
- 22 Larsson, R., Larsson, P. O., Eriksson, E., Sjöberg, M. and Höglund, E. Lubricant properties for input to hydrodynamic and elastohydrodynamic lubrication analyses. *Proc. Instn Mech. Engrs, Part J, Journal of Engineering Tribology*, 2000, **214**(J1), 17–28.
- 23 Sharif, K. J., Kong, S., Evans, H. P. and Snidle, R. W. Contact and elastohydrodynamic analysis of worm gears. Part 2: results. *Proc. Instn Mech. Engrs, Part C, Journal of Mechanical Engineering Science*, 2001, **215**(C7), 831–846.
- 24 Kong, S., Sharif, K. J., Evans, H. P. and Snidle, R. W. Elastohydrodynamics of a worm gear contact. *Trans. ASME, J. Tribology*, 2001, **123**, 268–275.

## APPENDIX

## Lubricant properties assumed in the analysis

Lubricant properties are pressure and/or temperature dependent according to the following formulae (subscript 0 represents the value at zero pressure and reference temperature  $\theta_0$ ):

$$\frac{\rho(p, \theta)}{\rho_0} = \left(1 + \frac{D_1 p}{1 + D_2 p}\right) [1 - \varepsilon(\theta - \theta_0)]$$

where

$$D_1 = 0.67 \text{ GPa}^{-1} \quad \text{and} \quad D_2 = 2.68 \text{ GPa}^{-1}$$

$$\varepsilon = \varepsilon_0 e^{-\lambda p} \quad \text{where } \lambda = 1.5 \text{ GPa}^{-1}$$

$$k = k_0 \left(1 + \frac{C_1 p}{1 + C_2 p}\right)$$

where

$$C_1 = 1.56 \text{ GPa}^{-1} \quad \text{and} \quad C_2 = 0.61 \text{ GPa}^{-1}$$

$$c(p, T) = \frac{\rho_0}{\rho} c_0 [1 + b_0(1 + b_1 p + b_2 p^2)(\theta - \theta_0)] \\ \times \left(1 + \frac{K_1 p}{1 + K_2 p}\right)$$

where

$$b_0 = 3.4 \times 10^{-4}, \quad b_1 = 3.3 \text{ GPa}^{-1}, \quad b_2 = -2.3 \text{ GPa}^{-2}$$

$$K_1 = 0.5 \text{ GPa}^{-1} \quad \text{and} \quad K_2 = 0.51 \text{ GPa}^{-1}$$